Applied Nanoscience
https://doi.org/10.1007/s13204-019-01062-w

ORIGINAL ARTICLE

Ni–Zn hydroxide-based bi-phase multiscale porous nanohybrids: physico-chemical properties

N. Habib[1,2] · O. Guellati[1,2,3] · A. Harat[1] · A. Nait-Merzoug[1,2] · J. El Haskouri[5] · D. Momodu[4] · N. Manyala[4] · D. Begin[3] · M. Guerioune[1]

Received: 31 July 2018 / Accepted: 18 May 2019

Abstract
In this investigation, we report the synthesis of novel homogeneous micro–mesoporous bi-phase nanohybrids based on Ni/Zn hydroxides using a simple and low-cost free-template urea-based hydrothermal process at two different growth temperatures (120 and 180 °C) for 6 h in two cases of precursor ratios (Ni:Zn = 1:1 and Ni:Zn = 1:2). The synthesized products have been characterized with different techniques such as XRD, FT-IR, FESEM, Raman, BET and XPS analysis to identify quantitatively and qualitatively their original physico-chemical properties. The obtained structural results show the formation of bi-hydroxide-based products: α^{*}-Ni(OH)$_2$·0.75 H_2O with $Zn_5(CO_3)_2(OH)_6$ (case Ni:Zn = 1:1) or with $Zn_4(CO_3)(OH)_6{\cdot}H_2O$ (Ni:Zn = 1:2) which are also proven by FTIR and Raman analyses. However, the obtained 3D micro–meso-nanohybrids with different pore morphology have been demonstrated through the FESEM micrographs depending on the synthesis conditions. Moreover, these porous products have been subjected to textural studies with the BET results showcasing a porous morphology with a reasonable specific surface area (SSA) and pore volume in the range (70–150 m^2/g) and (0.19–0.85 cm^3/g), respectively. Also, a clear improvement in the BET SSA (two times the initial value) was obtained with increasing the growth temperature in the two cases (1:1 and 1:2). Consequently, we have successfully synthesized active mesoporous materials with interesting specific surface area and porosity (pore volume and size) which make them attractive materials for electrode applications especially in energy storage and biosensing.

Keywords Micro–mesoporous materials · Layered double hydroxides · Micro-nanohybrid · Free-template hydrothermal synthesis · Porosity

Introduction

Nanoporous structured hydroxide-based nanohybrids, precisely transition metal hydroxide-based nanomaterials, have attracted much attention as a promising and active material choice in large-scale applications such as molecular adsorption/storage and separation for environment, ion exchange, nanotechnology, supercapacitor for energy storage and conversion, electro-biosensing, and catalysts (Bardé et al. 2006; Li et al. 2016; Gobal and Faraji 2013), due to their unique properties which are strongly influenced by their composition, microstructure, and synthesis method (Mereu et al. 2013; Choy et al. 1998; Li et al. 2015; Hu et al. 2008).

These kinds of nanomaterials possess high specific surface area, well-defined pore size distribution, and morphology as well as functional sites. Moreover, these porous materials can be classified as microporous (less than 2 nm), mesoporous (in the range of 2–50 nm) and macroporous

✉ O. Guellati
guellati23@yahoo.fr

1 Laboratoire d'Etude et de Recherche des Etats Condensés (LEREC), Département de Physique, Université Badji-Mokhtar de Annaba, BP. 12, 23000 Annaba, Algeria

2 Université Mohamed Cherif Messadia de Souk Ahras, Fac. Sci, BP. 1553, 41000 Souk-Ahras, Algeria

3 Institut de Chimie et Procédés pour l'Energie, l'Environnement et la Santé (ICPEES)-ECPM-CNRS-UdS, 25 rue Becquerel, 67087 Strasbourg Cedex 2, France

4 Department of Physics, Institute of Applied Materials, SARCHI Chair in Carbon Technology and Materials, University of Pretoria, Pretoria 0028, South Africa

5 Instituto de Ciencias de los Materiales de la Universitat de València. C/Catedrático José Beltrán, 2. Paterna, 46980 Valencia, Spain

Published online: 25 May 2019

(greater than 50 nm) with respect to their pore diameters (Gao et al. 2014). In recent years, mesoporous materials have been the focus of scientists due to textural properties which are aligned with the application requirements from these diverse fields.

Numerous methods have been proposed for the synthesis of mesoporous nanostructures with controllable size, shape, and chemical stability such as hydrothermal process, sol–gel, chemical impregnation (Li et al. 2015; Byrappa and Adschiri 2007; Lontio Fomekong et al. 2015; Zhong et al. 2005; Liu et al. 2015). Moreover, the chemical and physical properties of these nanomaterials not only depend on their size, morphology and phase structure but also are influenced by their composition. Recent efforts have been focused on transition metal hydroxide nanocomposites with mixed metals taking into account their own properties. Among them, nickel- and zinc-based hydroxide nanomaterials have not been systematically studied for their large-scale applications (Zheng et al. 2017; Lai et al. 2017; Jian et al. 2017) as capacitor electrodes which are one of the oldest but still promising electrochemical energy storage solutions for hybrid electric vehicles and portable electrical/electronic devices.

In this work, we report the successful synthesis of metallic (Ni or Zn)-based carbonate $(CO_3)^{2-}$ and/or hydroxide $(OH)^-$ bi-structures in micro–nanoporous spheric nanohybrids using a simple one-step free-template urea-based hydrothermal method, which has high efficiency and is a low-cost growth process. Furthermore, the present work is a novel report which provides a detailed and systematic approach to investigate the structural, morphological and electrochemical characteristics of Ni–Zn-based bi-transition metal hydroxides.

Experimental procedure

All the chemicals, urea (Merck, purity ≥ 98%), and nickel and zinc chlorides (Sigma-Aldrich, purity ≥ 99.99%), were of analytical grade and were used without further purification.

Ni–Zn carbonate and/or hydroxide-based heterostructure nanohybrid synthesis

0.1 M nickel (II) chloride hexahydrate ($NiCl_2.6H_2O$) and 0.1 M zinc (II) chloride ($ZnCl_2$) were dissolved in deionised water at room temperature (25 °C). After that, 0.5 M urea (CH_4N_2O), which is highly soluble in water, was added into the above solution and ultrasonicated for 30 min until a dark green transparent solution was obtained which was transferred into a 40-mL Teflon-lined hydrothermal autoclave system. The autoclave was sealed, maintained at two different growth temperatures (120 and 180 °C) for 6 h and then cooled down naturally to room temperature. The obtained products with different colors were filtered and washed with distilled water and ethanol several times, before drying in an oven at 80 °C overnight. Thereafter, a series of 3D crystalline heterometallic Ni–Zn hydroxide nanohybrids were synthesized using a free-template hydrothermal process by changing the Ni–Zn precursor ratios (1:1 and 1:2) and growth temperature with keeping the same experimental conditions. The corresponding samples were designated as Ni-xZn-y °C (where $x = 1$ or 2; y = temperature growth).

Characterization techniques

The synthesized bi-phase nanohybrids were systematically characterized by several analytical methods to study the effect of the hydrothermal process parameters on the products structural, morphology, and composition which have an influence on their electrochemical performance.

The structural characterization of Ni–Zn carbonate and/or hydroxide-based nanohybrids were investigated by powder X-ray diffraction (XRD) using a XRD D8 ADVANCE-BRUKER AXS diffractometer, equipped with a copper anticathode tube ($\lambda_{CuK\alpha} = 1.5406$ Å) and a graphite monochromator rear blade, operating at 40 kV–40 mA and employing a scanning rate of $0.2°s^{-1}$. The XRD patterns of all specimens were recorded in the 2θ range of 10–90°.

The nanohybrid morphology was obtained using a field-emission scanning electron microscopy (FESEM) (JEOL 6700-FEG microscope) operated at 3 kV.

Raman scattering measurements were carried out at room temperature with a Horiba JobinYvon Lab-RAM Aramis confocal Raman spectrometer equipped with a cooled CCD camera and an automated XYZ table, at a laser excitation of 532 nm. Using a D2 filter, the laser power that reached the samples was estimated as 0.33 mW.

Fourier-transform infrared (FTIR) spectra were recorded using a BrukerVertex 77v spectrometer in the 400–4000 cm^{-1} range with a 4-cm^{-1} resolution controlled with an Opus software analysis software.

The Brunauer–Emmett–Teller (BET)-specific surface area (SSA) measurements and the porosity distribution of the as-synthesized products were carried out on a Tristar an ASap2420 sorptometer (Micromeritics), using N_2 as adsorbent at liquid nitrogen temperature, through N_2 adsorption/desorption isotherms and the Barrett–Joyner–Halenda (BJH) method, respectively. Before measurements, the samples were initially out-gassed under vacuum overnight at room temperature to prevent material transformation and also to remove any impurities and moisture from the surface.

Surface chemical binding energies of the as-prepared layered double hydroxide (LDH)-based nanohybrids were performed using X-ray photoelectron spectroscopy in an ESCA + equipment by Omicron. The system is equipped

with a dual X-ray source ($Mg_{K\alpha}$ = 1253.6 eV for our analysis, $Al_{K\alpha}$ = 1486.6 eV), an electrostatic hemi-spherical analyzer and detector with 7 channel trons. Depth profiling was performed using the ion gun, and imaging (lateral resolution of 60 μ) and sample pretreatment were done in the reaction chamber. Binding energies were standardized by assigning the value of the C_{1s} peak to 284.6 ± 0.2 eV relative to the Fermi energy level. The fitting procedure and the asymmetric peak deconvolutions were made using the "XPS Peak Fit and Casa XPS" programs where a Shirley background has been used and the Lorentzian–Gaussian (L/G) ratio was fixed at 30%. It is a reliable technique to study the chemical states of bonded Ni–Zn elements on the surfaces of our nanohybrids by measuring their binding energy.

Results and discussion

Structural properties

In this investigation, we start with the purity and the phase structure identification of our products. Figure 1 shows the powder XRD diffractograms of our products obtained using two different precursor ratios and growth temperatures with their Inorganic Crystal Structure Database (ICSD) reference cards. The most obtained characteristic sharp and symmetric peaks show a typical XRD pattern of combination of two different transition metal hydroxide structures inside the synthesized nanohybrids with more nanocrystalline nature.

As a result, samples with equimolar Ni–Zn precursors (1:1 ratio shown in Fig. 1a), synthesized at 120 °C and 180 °C for a 6-h period can be indexed to a typical rhombohedral lattices of nickel hydroxide hydrate (α*-Ni-HH) (α*-$Ni(OH)_2{\cdot}0.75\ H_2O$) and zinc carbonate hydroxide (Zn-CH) ($Zn_5(CO_3)_2(OH)_6$) depending on the reference cards [JCPDS 038-0715] and [JCPDS 19-1458], respectively. The diffraction peaks at 11.11°, 21.99°, 33.50° and 60.18° correspond to the α*-Ni-HH (003), (006), (101) and (110), respectively (Huang et al. 2015).

The existence of sharp peaks at 13.09°, 28.49°, 33.47° and 35.86° are attributed to the crystalline Zn-CH corresponding to (200), (020), (002) and (510) planes, respectively. This indexing clearly depicts a typical profile of layered hydroxide-based material (Choy et al. 1998; Li et al. 2015; Rojas et al. 2008; Huang et al. 2015) with the interlayer anions and their crystalline parameters as reported in Table 1, as well as the values of the $d_{(001)}$ which determine the thickness of the brucite-like layer. From the first (003) peak position at a 2θ-value of approximately 11.11°, an interlayer distance of 7.77 Å could be estimated, which is in good agreement with those reported in the literature [7.79 Å for the spacing in α*-$Ni(OH)_2{\cdot}0.75\ H_2O$ phase (Huang et al. 2015)].

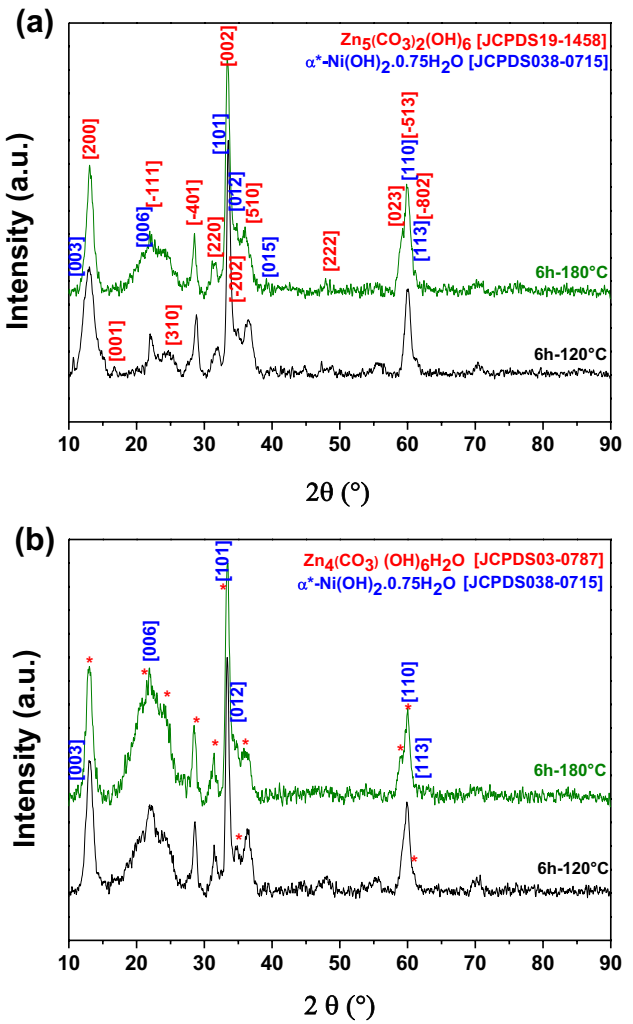

Fig. 1 XRD patterns of obtained Ni–Zn [1:1 (**a**) and 1:2 (**b**)] bi-phase nanohybrids using urea-based hydrothermal process with different experimental parameters

However, the XRD diffraction patterns of the second Ni–Zn precursors with a 1:2 ratio (Fig. 1b) correspond to the same α*-Ni hydroxide (α*-Ni-HH) phase but accompanied with another different Zn phase which is the zinc carbonate hydroxide hydrate (Zn-CHH) $Zn_4(CO_3)(OH)_6{\cdot}H_2O$ depending on the reference card [JCPDS 03-0787]. These patterns are characterized by an intense peak at 12.92° and with some others weak diffraction peaks at 21.85° and 33.31° confirming the layered structure (Choy et al. 1998).

Thus, from the XRD analysis, it is worthy to state that the sample with precursor ratio of 1:1 gave a bi-structure rich with carbonate in comparison with the sample with the Ni–Zn precursor ratio of 1:2 which contains more hydroxides (LDH-type structure) depending on the peak intensities.

FTIR analysis was also carried out to clarify the existing chemical bonds (see Fig. 2). From the results obtained, there exists several vibration bands where the key bands resemble

Table 1 Physico-chemical characteristics of the synthesized bi-hydroxide-based 3D micro-nanohybrids

Bi-phase nanostructure	Crystalline parameters (Å)	BET-SSA (m^2/g)	BJH pore vol. (cm^3/g)	Pore diam. (nm)
1/1 α^*-Ni-HH + Zn_5 CH				
(A)	$a = 3.10$ Å, $c = 24.11$ Å $a' = 13.85$ Å, $b' = 6.19$ Å, $c' = 5.48$ Å, $\beta = 101°$	51.57	0.16	12.35
(B)	$a = 3.11$ Å, $c = 24.22$ Å $a' = 13.72$ Å, $b' = 6.24$ Å, $c' = 5.51$ Å, $\beta = 100.1°$	126.70	0.66	20.81
1/2 α^*-Ni-HH + Zn_4 CHH				
(C)	$a = 3.11$ Å, $c = 24.22$ Å –	61.08	0.19	12.18
(D)	$a = 3.10$ Å, $c = 24.44$ Å –	105.25	0.85	32.40

6 h–120 °C (A and C), 6 h–180 °C (B and D)

α^*-Ni-HH (α^*-$Ni(OH)_2 \cdot 6\ H_2O$) ($a = 3.08$ Å and $c = 23.41$ Å), Zn_5CH ($Zn_5(CO_3)_2(OH)_2$) ($a' = 13.58$ Å, $b' = 6.28$ Å, $c' = 5.41$ Å, $\beta = 95.6°$), Zn_4 CHH ($Zn_4(CO_3)(OH)_6 \cdot H_2O$) (crystalline parameters not found)

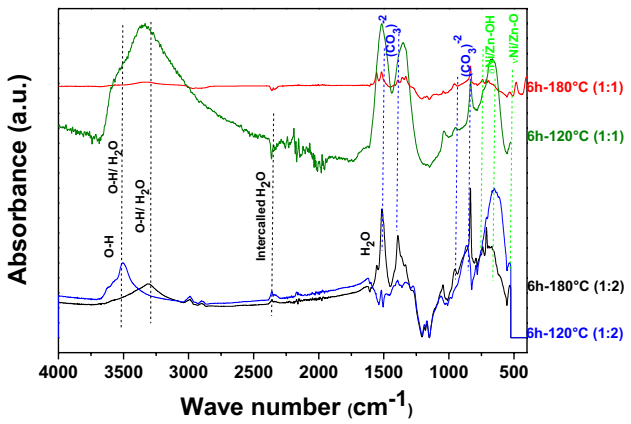

Fig. 2 FTIR spectra of obtained Ni–Zn bi-phase nanohybrids using urea-based hydrothermal method with different experimental parameters

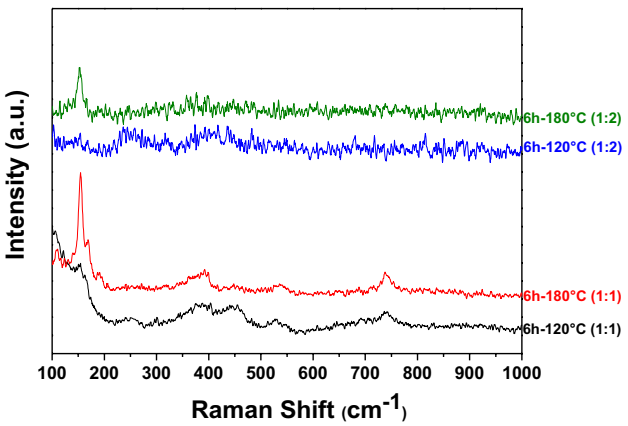

Fig. 3 Raman spectroscopy spectra of Ni–Zn (1:1 and 1:2)-based heterostructure hydroxides synthesized by hydrothermal method at two different growth temperatures

those exhibited by hydrotalcite-like phase with CO_3^{2-} as the counter anion (Buazar et al. 2016). An intense broad absorption band centered at 3450 cm^{-1} was observed for the sample synthesized at 180 °C with a precursor molar ratio of 1:2 and 3500 cm^{-1} for the same sample synthesized at 120 °C. This is attributed to the stretching vibrations of the hydroxyl groups (O–H vibration) found on the surface and at the interlayer water molecules; this is also observed in the LDH materials and is comparable with the OH stretching vibration in free water active at 3600 cm^{-1} (Rojas et al. 2004; Xie et al. 2015; Ashassi-Sorkhabi et al. 2016). The broad band at 3141 cm^{-1} accompanied by nearby band at 3023 cm^{-1} can be assigned to the hydrogen bonding between water and carbonate in the LDH interlayer. The band at 1605 cm^{-1} is assigned to the bending vibration of water molecules (Rojas et al. 2004; Ashassi-Sorkhabi et al. 2016; Kotteeswaran et al. 2017; Wang et al. 2015).

In most of hydrotalcites, there are three IR active absorption bands arising from the carbonate anion observed at 1384 cm^{-1} (υ_3), 1058 cm^{-1} (υ_1) and 745 cm^{-1} (υ_2) (Kotteeswaran et al. 2017). The bands at 996 cm^{-1} and 826 cm^{-1} are associated with metal–oxygen (M–O) and metal–hydroxyl (M–OH) groups in the lattice of LDHs (M can be Ni or Zn) (Rojas et al. 2004). Moreover, the sharp band at 835 cm^{-1} is associated with in-plane quadrant bending (Li et al. 2015). Another peak at 1109 cm^{-1} is associated with C–O single-bond stretching vibrations. In addition, below 646 cm^{-1}, the obtained bands are attributed to δNi/Zn-OH or ν Ni/Zn-O as reported in many studies (Wang

et al. 2015; Buazar et al. 2015, 2016; Koopi and Buazar 2018).

The Raman spectroscopy studies are shown in Fig. 3 to confirm the previous results. In detail, the spectra consisted of Raman-active bands at 106, 153, 392, 448, (525–543) and 737 cm^{-1}. The bands at 392, 448 and in the range (525–543 cm^{-1}) indicate the presence of a theophrastite $Ni(OH)_2$ phase depending to the reference (RRUFF ID: R070699) (Mohapatra et al. 2017; Ramadoss et al. 2016). Furthermore, the indexed peaks around 153 and 737 cm^{-1} show very good agreement with the reported values for hydrozincite $Zn_5(CO_3)_2(OH)_2$-based nanomaterial depending on the reference (RRUFF ID: R050635). More precisely, the band located in the range (525–543 cm^{-1}) can be assigned to the vibrations of the NiO/ZnO symmetric stretching (A_g) mode (Mohapatra et al. 2017). However, the peak located at 448 cm^{-1} corresponds to a Ni-OH/Zn-OH symmetric (A_{1g}(T)) mode and an apparent band at 153 cm^{-1} is indicative of (E_g) symmetry mode (Mohapatra et al. 2017).

Studies by Mohapatra et al. (2017), indicate that Raman peaks observed at 106, 392, 448 and [525–543 cm^{-1}] could be linked to the E_{2l}, E_{2h}, E_{2l}, E_{2h} and A_l(LO) multi-phonon modes, respectively. In general, a group theory analysis of the phonon modes in brucite-type hydroxides predicts that four Raman active modes are found, three of which are lattices mode in the range (310–530 cm^{-1}) and one is a symmetric OH stretching vibration at around 3581 cm^{-1} (Mohapatra et al. 2017; Ramadoss et al. 2016; Oyedotun et al. 2018). Thus, these results suggest also the formation of bi-phase nanohybrids based of Ni hydroxide and Zn carbonate hydroxide which is in agreement with the XRD and FTIR results.

Morphological and textural properties

FESEM results

Figure 4 shows the FESEM micrographs of these synthesized bi-phase nanohybrids with different quasi-microspherical framework (ranging from 6 to 25 µm) based on regular or irregular nanoflake-like and sponge-shaped morphologies depending on the precursor ratio and growth temperature. The formation of very interesting 3D hierarchical micro/nanostructures with different kinds of textural pores depending on the hydrothermal synthesis conditions is illustrated. The Ni ions might have lowered the surface energy difference between the polar and nonpolar planes, leading to distinct morphologies (Kim et al. 2017). However, with an increase in the amount of Zn precursor into the Ni solution in twofold (Fig. 4c, d), layered plate-like particles and individual spherical structures that were interconnected without clear boundaries formed continuous nanolayered structures, respectively. Notably, this kind of porous structure is favorable for efficient and fast ion transport to the surface of the active materials, which is interesting for the utilization of these active materials in specific conditions.

BET analysis results

Figure 5 shows the N_2 adsorption/desorption isotherms and their corresponding BJH pore size distribution plots of the as-prepared bi-phase nanohybrids. It can be seen that these isotherms are typical Langmuir type IV characteristic according to IUPAC classification with an obvious hysteresis loop at a relative pressure (P/P_0) between 0.4 and 1.0, which indicates the existence of mesoporous structures (Wang et al. 2015; Hu et al. 2017).

The corresponding BET-SSA was determined to be in the range (52–127 $m^2\ g^{-1}$) with an average pore size and volume in the range (12–32 nm) and (0.16–0.85 $cm^3\ g^{-1}$), respectively, as reported in Table 1. In addition, with this quantitative analysis, we can clearly see the effect of the synthesis temperature. The SSA value increases to double the original value with increasing the hydrothermal synthesis temperature from 120 to 180 °C.

Therefore, these mesoporous nanostructures with a large surface area confirm their importance in a wide range of applications. More precisely, these nanoscale distributed pores would favor, for example, the fast diffusion of the electrolyte ions into these electroactive materials which will be used in our perspective investigation using these hydroxides as electroactive for supercapacitors.

XPS spectroscopy surface analysis results

To explore the surface elemental composition, the chemical valences and the oxidation states of bonded elements, the synthesized NiHH/ZnCH micro-nanosystems at different hydrothermal growth temperatures and precursor ratios were also studied and the corresponding binding energy (BE) values are shown in Fig. 6.

In Fig. 6a, the survey scan spectra for all the synthesized samples depict the presence of Ni, Zn, C and O elements at their signatory binding energy position. Figure 6b displays the different percentage composition content of the deconvoluted parameters for the different synthesis conditions. In addition, we present the deconvolution of main spectra regions at high-resolution core level spectra of the Ni_{2p}, Zn_{2p}, C_{1s}, and O_{1s} for all samples, using a L/G fitting method where the fitting parameters found on these spectra (binding energy, asymmetry of the main peak, intensity ratio between the main and the satellite peaks) are consistent with the literature data (see Fig. 7). Moreover, as reported in Fig. 6b, the area ratio of Zn_{2p} and Ni_{2p} in the products is around 0.6–0.89

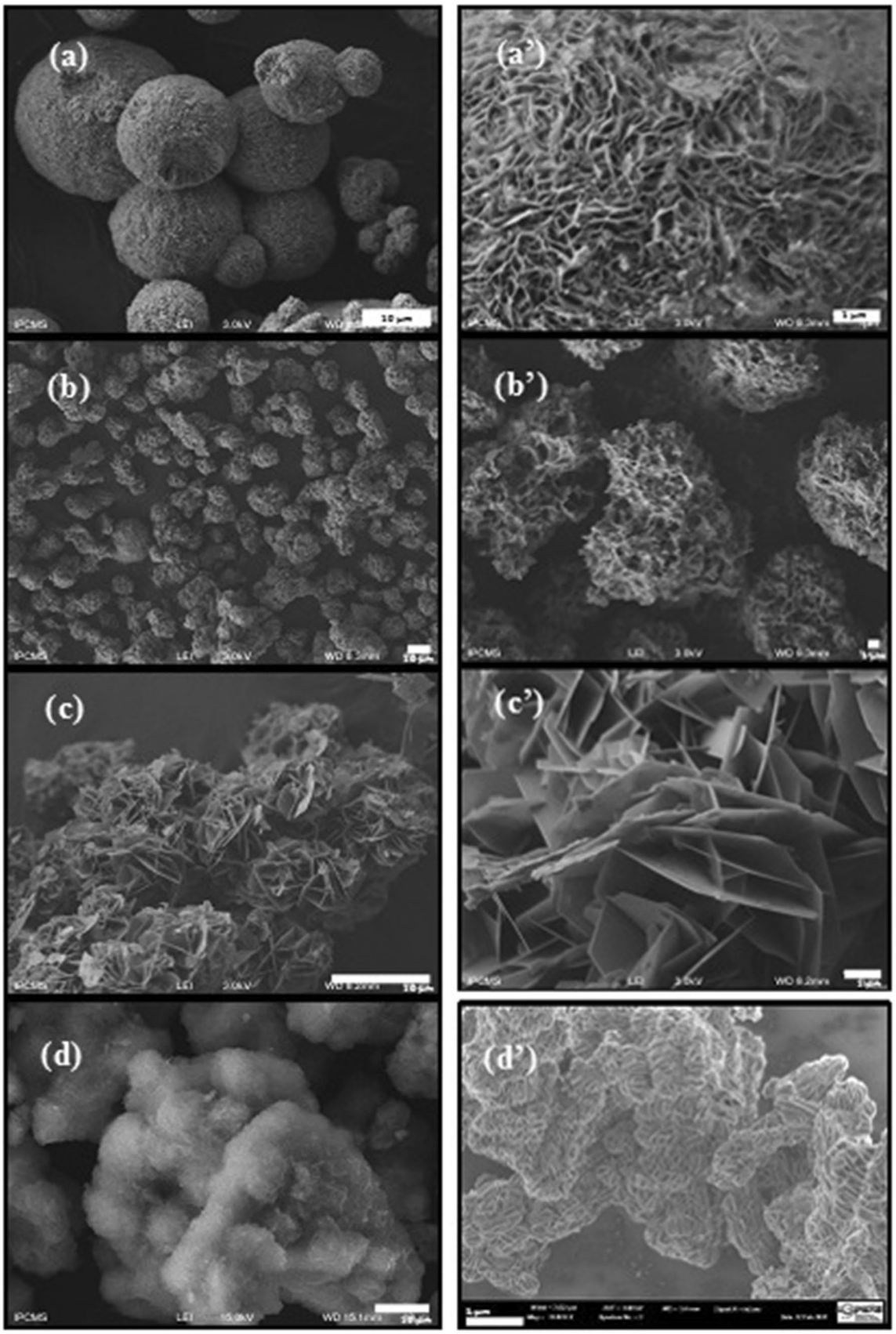
(a)
(a')
(b)
(b')
(c)
(c')
(d)
(d')

◂**Fig. 4** FESEM micrographs of obtained micro-nanostructures based of Ni–Zn bi-phase nanohybrids at two different growth temperatures and Ni:Zn precursor ratios: 1:1 (**a.a'.** 6 h–120 °C, **b.b'.** 6 h–180 °C), 1:2 (**c.c'.** 6 h–120 °C, **d.d'.** 6 h–180 °C)

and 1.2–1.5, respectively, for the Ni/Zn precursor ratios of 1:1 and 1:2 which agree with the nanostucture composition.

In the Ni_{2p} high-resolution spectrum, not only two main peaks with binding energy around 854.1–857.6 eV and 861.6–867.3 eV associated with Ni^{2+} spin–orbit are found,

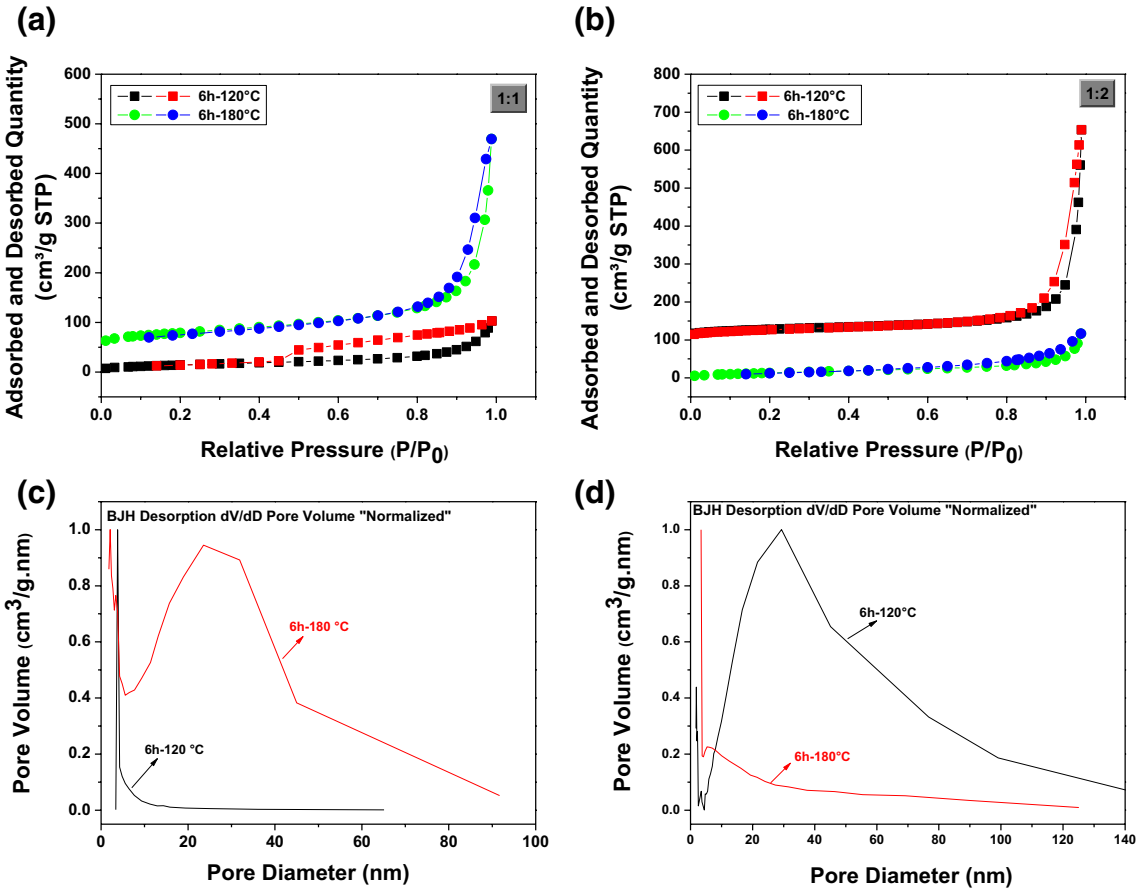

Fig. 5 N_2 adsorption–desorption isotherms (up) and the corresponding pore size distribution (down) of the synthesized Ni–Zn-based micro-nanostructures using hydrothermal method at two different growth temperatures and Ni/Zn precursor ratios

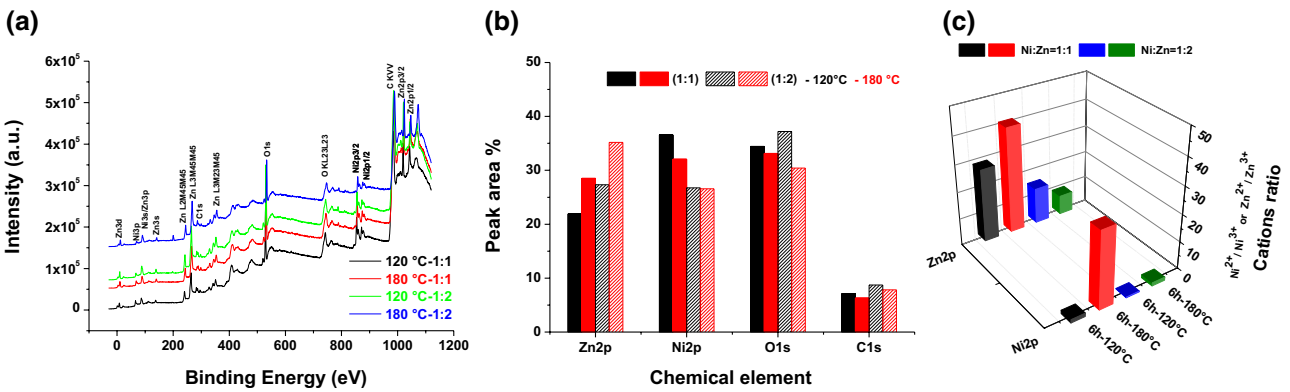

Fig. 6 XPS survey scan spectra (**a**) and percentage composition depending to the synthesis condition (**b**, **c**)

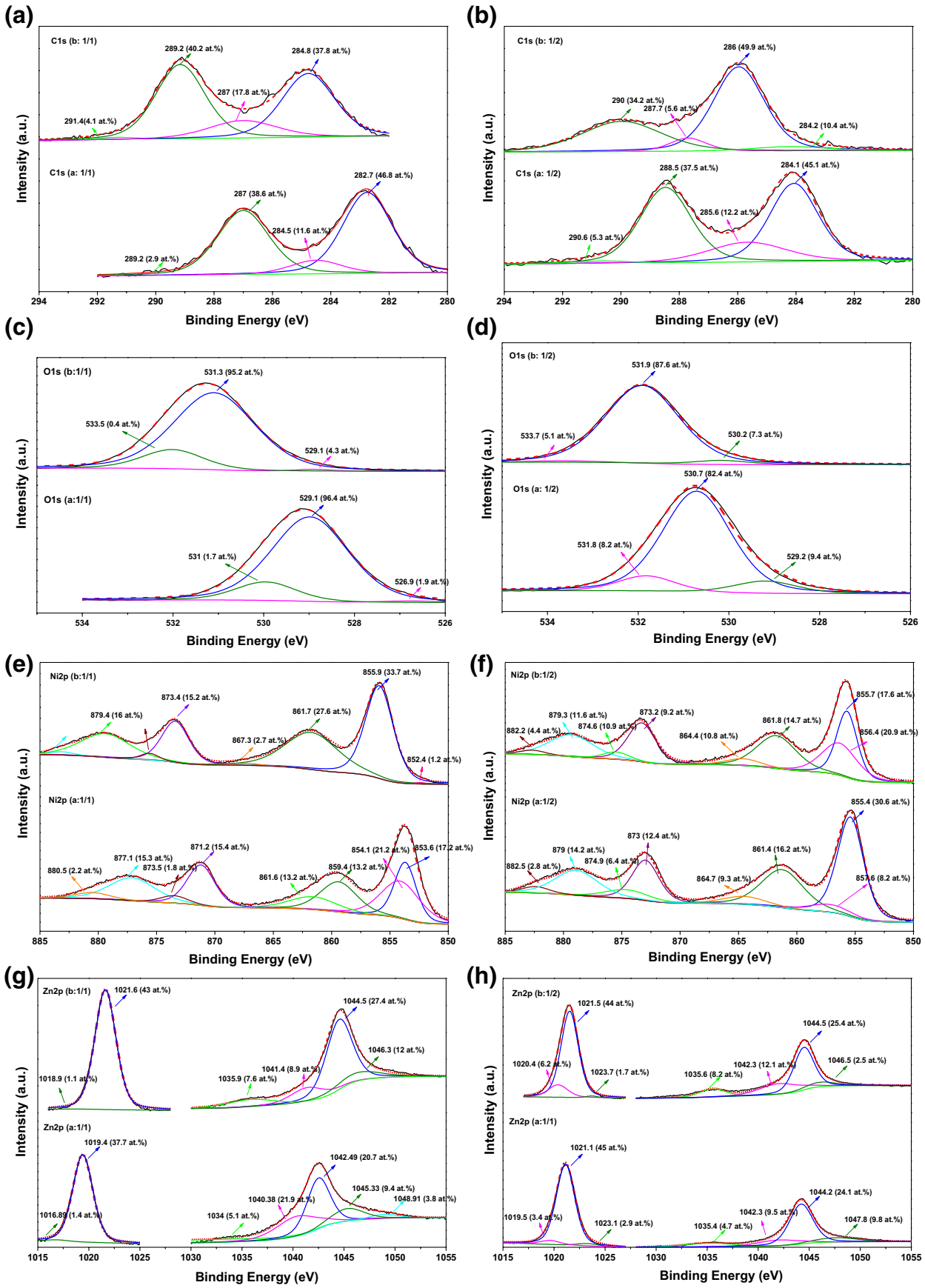
(a)
C1s (b: 1/1)
289.2 (40.2 at.%)
284.8 (37.8 at.%)
287 (17.8 at.%)
291.4(4.1 at.%)
C1s (a: 1/1)
287 (38.6 at.%)
282.7 (46.8 at.%)
284.5 (11.6 at.%)
289.2 (2.9 at.%)
Intensity (a.u.)
Binding Energy (eV)
(b)
C1s (b: 1/2)
286 (49.9 at.%)
290 (34.2 at.%)
287.7 (5.6 at.%)
284.2 (10.4 at.%)
C1s (a: 1/2)
288.5 (37.5 at.%)
284.1 (45.1 at.%)
285.6 (12.2 at.%)
290.6 (5.3 at.%)
(c)
O1s (b:1/1)
531.3 (95.2 at.%)
533.5 (0.4 at.%)
529.1 (4.3 at.%)
O1s (a:1/1)
529.1 (96.4 at.%)
531 (1.7 at.%)
526.9 (1.9 at.%)
(d)
O1s (b: 1/2)
531.9 (87.6 at.%)
533.7 (5.1 at.%)
530.2 (7.3 at.%)
O1s (a: 1/2)
530.7 (82.4 at.%)
531.8 (8.2 at.%)
529.2 (9.4 at.%)
(e)
Ni2p (b:1/1)
855.9 (33.7 at.%)
873.4 (15.2 at.%)
879.4 (16 at.%)
861.7 (27.6 at.%)
867.3 (2.7 at.%)
852.4 (1.2 at.%)
Ni2p (a:1/1)
871.2 (15.4 at.%)
877.1 (15.3 at.%)
854.1 (21.2 at.%)
853.6 (17.2 at.%)
880.5 (2.2 at.%)
873.5 (1.8 at.%)
859.4 (13.2 at.%)
861.6 (13.2 at.%)
(f)
Ni2p (b:1/2)
855.7 (17.6 at.%)
879.3 (11.6 at.%)
873.2 (9.2 at.%)
882.2 (4.4 at.%)
874.6 (10.9 at.%)
861.8 (14.7 at.%)
856.4 (20.9 at.%)
864.4 (10.8 at.%)
Ni2p (a:1/2)
855.4 (30.6 at.%)
873 (12.4 at.%)
879 (14.2 at.%)
861.4 (16.2 at.%)
882.5 (2.8 at.%)
874.9 (6.4 at.%)
857.6 (8.2 at.%)
864.7 (9.3 at.%)
(g)
Zn2p (b:1/1)
1021.6 (43 at.%)
1044.5 (27.4 at.%)
1046.3 (12 at.%)
1018.9 (1.1 at.%)
1041.4 (8.9 at.%)
1035.9 (7.6 at.%)
Zn2p (a:1/1)
1019.4 (37.7 at.%)
1042.49 (20.7 at.%)
1045.33 (9.4 at.%)
1040.38 (21.9 at.%)
1048.91 (3.8 at.%)
1016.89 (1.4 at.%)
1034 (5.1 at.%)
(h)
Zn2p (b:1/2)
1021.5 (44 at.%)
1044.5 (25.4 at.%)
1020.4 (6.2 at.%)
1023.7 (1.7 at.%)
1042.3 (12.1 at.%)
1046.5 (2.5 at.%)
1035.6 (8.2 at.%)
Zn2p (a:1/1)
1021.1 (45 at.%)
1044.2 (24.1 at.%)
1019.5 (3.4 at.%)
1023.1 (2.9 at.%)
1042.3 (9.5 at.%)
1047.8 (9.8 at.%)
1035.4 (4.7 at.%)

◂**Fig. 7** XPS spectra of these Ni–Zn bi-hydroxides micro-nanosystems in the Ni_{2p}, Zn_{2p}, C_{1s}, and O_{1s} energy regions at different conditions: (**a**: 6 h/120 °C and **b**: 6 h/180 °C)

but also peaks around 853.6–855.7 eV and 859.4–861.8 eV are fitted to be associated with Ni^{3+} spin–orbit indicating the presence of elemental Ni in the formation of $Ni(OH)_2$ hydroxide with some traces of metal Ni around 852.4 eV in some cases (Li et al. 2015; Kim et al. 2017; Hu et al. 2017; Wang et al. 2017). This high-resolution scan also contains their two corresponding satellite peaks at around 873 eV and 879 eV with considerable intensities also found in many other related studies (Wang et al. 2015; Kim et al. 2017; Wang et al. 2017; Fu et al. 2016; Li et al. 2017a, b). These spin–orbit coupling with splitting energy gap of 17.6 ± 0.2 eV corresponds to two major peaks $Ni_{2p3/2}$ and $Ni_{2p1/2}$, respectively, with two kinds of Ni species as reported by several works (Wang et al. 2015; Ede et al. 2017). Furthermore, we can clearly show that these Ni–Zn-based hydroxide BE are shifted in comparison with values found in the literature with Ni–Fe (Li et al. 2015; Chen et al. 2016), Ni–Co (Li et al. 2015, 2017a; b; Chen et al. 2016), and Ni–Al (Li et al. 2017a) hydroxide-based nanocomposites.

Similarly, in the region of Zn_{2p} peaks, two spin–orbit doublets with their own adjacent obvious two apparent satellites (Sat.) were observed and the dominant fitted peaks centered around 1021 ± 1 eV and 1043 ± 1 eV could be ascribed to $Zn_{2p3/2}$ and $Zn_{2p1/2}$ (Zn-OH-related binding states), respectively, of mostly Zn^{2+} oxidation state with a spin energy separation of 23 ± 0.1 eV (Wang et al. 2015, 2017; Mohamed et al. 2017). We also found some traces of Zn-OOH and O-deficient Zn^{1+} centered around 1023 eV and 1019 ± 1 eV, respectively, as reported in the work by Wang et al. (2017).

Consequently, Ni_{2p} and Zn_{2p} show that the oxidation state of these elements is the mixed state of two kinds of ions, namely Ni^{2+} (or Zn^{2+}) and Ni^{3+} (or Zn^{3+}), respectively, with different ratios as reported in Fig. 6c which agrees with those reported in other previous reports (Liang et al. 2016).

In the case of the C_{1s} core level spectrum recorded, this was attributed to the samples containing the carbonate structural phase or signals picked up from the adhesive-carbon tape used as substrate during the XPS analysis. Different carbon-containing groups were obtained which include the C–C at 282.7 eV, C=C at 284.5 ± 0.3 eV (non-oxygenated ring C), C–O (C–OH) at 286 eV (C in C–O bonds), C=O at 287 eV (carbonyl), O–CO around 288.2 ± 0.3 eV (carboxylate carbon) and (O–C=O) around 291 ± 1 eV (Li et al. 2017a, b). The predominant presence of the C=O, C–O and the O–H bonds confirm that the sample contains hydroxyl and carbonate groups with different percentages depending on the synthesis conditions.

In addition, the core level O_{1s} peaks found in these carbonate hydroxides are ascribed to the presence of a strong pronounced peaks centered around 529 ± 1 eV and 531 ± 0.3 eV illustrating the divalent state of O bonded as hydroxide (OH^-) groups (Li et al. 2017a, b).

It can also be bonded with metals to form metal oxides (O-M) and hydroxides (M-OH) (with M: Zn or Ni) (Wang et al. 2015, 2017; Li et al. 2015).

The binding energy peak at 531.7 and 533.6 ± 0.1 eV appeared even more with second series of products (Ni:Zn = 1:2), which can be assigned to the contributions of adsorbed or crystal water (Li et al. 2015). In particular, the recorded OH area was between 82 and 95 at.% of the total O_{1s} peak area which gives a balances between dominate (OH^-) hydrate and carbonate hydroxide (Wang et al. 2017).

Consequently, these detailed reliable XPS analysis supports the previous results obtained from XRD and FTIR emphasizing the formation of pure Ni–Zn carbonate hydroxide nanohybrids with intercalated carbonate ions with different NiHH–ZnCH phase ratios and Ni^{2+}/Ni^{3+} (or Zn^{2+}/Zn^{3+}) ion ratios depending on the hydrothermal synthesis conditions. These results confirm that strong electron interactions occurred between Ni and Zn in this bi-hydroxide nanohybrid configuration.

Conclusion

In this investigation, the initial part of the work reports on bi-structural Ni–Zn carbonate hydroxide-based micro-nanohybrid synthesis using a simple and low-cost hydrothermal process focusing mainly on the growth temperature and Ni–Zn precursor ratio effect on the structural, textural and morphological selectivity of the synthesized nanohybrids.

Therefore, the obtained results confirm the production of multiscale porous hydroxide-based nanohybrids with regular or irregular nanoflake-like and sponge-shaped morphologies in 3D hierarchical micro/nanostructures with different kinds of textural pores depending on the optimized hydrothermal synthesis conditions. The oxidation state in these products is the mixed state of two kinds of anions, namely Ni^{2+} (or Zn^{2+}) and Ni^{3+} (or Zn^{3+}), respectively, with different ratios depending to the growth conditions. These obtained morphological characteristics favor the electrolyte ion diffusion, enhance the charge transport and provide more electroactive sites for fast electron/ion transfer energy storage.

These obtained mesoporous 3D architecture bi-hydroxide nanohybrids possessed very interesting specific surface area (52–127 $m^2\ g^{-1}$) with reasonable pore volume (0.16–0.85 $cm^3\ g^{-1}$) and pore size distribution (12–32 nm) which can provide additional active sites to facilitate the rapid ion diffusion and penetration or electron/ion transfer.

Consequently, these hierarchically nano-porous transition bi-metal hydroxides and carbonate hydroxides structures based of Ni and Zn should be promising electroactive

materials in the fabrication of half-cell device electrodes for mostly energy storage, environment, and sensing applications in perspective.

Acknowledgements We express our gratitude and sincere thanks to Prof. C. Pham-Huu (Strasbourg ICPEES), Prof. Manyala group's (University of Pretoria), Prof. F. Antoni (ICUBE) and Dr. K. Parkhomenko (Strasbourg ICPEES), for their assistance in material analysis. The authors also thank the Algerian minister program for financial support.

References

Ashassi-Sorkhabi H, La'le Badakhshan P, Asghari E (2016) Electrodeposition of three dimensional-porous Ni/Ni(OH)$_2$ hierarchical nano composite via etching the Ni/Zn/Ni(OH)$_2$ precursor as a high performance pseudocapacitor. Chem Eng J 299(1):282–291. https://doi.org/10.1016/j.cej.2016.04.069

Bardé F, Palacín MR, Beaudoin B, Christian PA, Tarascon JM (2006) Cationic substitution in γ-type nickel (oxi) hydroxides as a means to prevent self-discharge in Ni/Zn primary batteries. J Power Source 160:733–743. https://doi.org/10.1016/j.jpowsour.2005.12.073

Buazar F, Bavi M, Kroushawi F, Halvani M, Khaledi Nasab A, Hossieni SA (2015) Potato extract as reducing agent and stabiliser in a facile green one-step synthesis of ZnO nanoparticles. J Exp Nanosci 11(3):1–10. https://doi.org/10.1080/17458080.2015.1039610

Buazar F, Baghlani-Nejazd MH, Badri M, Kashisaz M, Khaledi-Nasab A, Kroushaw F (2016) Facile one-pot phytosynthesis of magnetic nanoparticles using potato extract and their catalytic activity. Starch/Stärke 68:1–9. https://doi.org/10.1002/star.201500347

Byrappa K, Adschiri T (2007) Hydrothermal technology for nanotechnology. Prog Cryst Growth Charact Mater 53(2):117–166. https://doi.org/10.1016/j.pcrysgrow.2007.04.001

Chen J, Xu J, Zhou S, Zhao N, Wong CP (2016) Amorphous nanostructured FeOOH and Co-Ni double hydroxides for high-performance aqueous asymmetric supercapacitors. Nano Energy 21:145–153. https://doi.org/10.1016/j.nanoen.2015.12.029

Choy JH, Kwon YM, Han KS, Song SW, Chang SH (1998) Intra- and inter-layer structures of layered hydroxy double salts, $Ni_{1-x}Zn_{2x}(OH)_2(CH_3CO_2)_{2x}{\cdot}nH_2O$. Mater Lett 34:356–363

Ede SR, Anantharaj S, Kumaran KT, Mishra S, Kundu S (2017) One step synthesis of Ni/Ni(OH)$_2$ nano sheets (NSs) and their application in asymmetric supercapacitors. RSC Adv 7:5898–5911. https://doi.org/10.1039/C6RA26584G

Fu W, Wang Y, Han W, Zhang Z, Zha H, Xie E (2016) Construction of hierarchical $ZnCo_2O_4$@$Ni_xCo_{2x}(OH)_{6x}$ core/shell nanowire arrays for high-performance supercapacitors. J Mater Chem A 4:173–182. https://doi.org/10.1039/C5TA07965A

Gao F, Li WM, Hou YJ (2014) Investigation for mechanical properties of porous materials based on homogenization theory. Adv Mater Res 1048:414–417. https://doi.org/10.4028/www.scientific.net/AMR.1048.414

Gobal F, Faraji M (2013) Fabrication of nanoporous nickel oxide by dezincification of Zn–Ni/(TiO_2-nanotubes) for use in electrochemical supercapacitors. Electrochim Acta 100:133–139. https://doi.org/10.1016/j.electacta.2013.03.155

Hu B, Chen SF, Liu SJ, Wu QS, Yao WT, Yu SH (2008) Controllable synthesis of zinc-substituted α- and β-nickel hydroxide nanostructures and their collective intrinsic properties. Chem Eur J 14:8928–8938. https://doi.org/10.1002/chem.200800458

Hu W, Wei H, She Y, Tang X, Zhou M, Zang Z, Du J, Gao C, Guo Y, Bao D (2017) Flower-like nickel-zinc-cobalt mixed metal oxide nanowire arrays for electrochemical capacitor applications. J Alloys Compd 708(25):146–153. https://doi.org/10.1016/j.jallcom.2017.02.301

Huang J, Yang Z, Wang R, Zhang Z, Feng Z, Xie X (2015) Zn–Al layered double oxides as high-performance anode materials for zinc-based secondary battery. J Mater Chem A 3:7429–7436. https://doi.org/10.1039/c5ta00279f

Jian Y, Wang D, Huang M, Jia HL, Sun J, Song X, Guan M (2017) Facile synthesis of Ni(OH)$_2$/carbon nanofiber composites for improving NiZn battery cycling life. ACS Sustain Chem Eng 5:6827–6834. https://doi.org/10.1021/acssuschemeng.7b01048

Kim DY, Ghodake GS, Maile NC, Kadam AA, Sung Lee D, Fulari VJ, Shinde SK (2017) Chemical synthesis of hierarchical $NiCo_2S_4$ nanosheets like nanostructure on flexible foil for a high performance supercapacitor. Sci Rep 7:9764–9773. https://doi.org/10.1038/s41598-017-10218-z

Koopi H, Buazar F (2018) A novel one-pot biosynthesis of pure alpha aluminum oxide nanoparticles using the macroalgae *Sargassum ilicifolium*: a green marine approach. Ceram Int 44(8):8940–8945. https://doi.org/10.1016/j.ceramint.2018.02.091

Kotteeswaran P, Raju VB, Murugan A, Santosh MS, Nagaswarupa HP, Prashantha SC, Kumar MA, Shivakumar MS (2017) Influence of zinc additive and pH on the electrochemical activities of β-nickel hydroxide materials and its applications in secondary batteries. J Energy Storage 9:12–24. https://doi.org/10.1016/j.est.2016.11.001

Lai SB, Jamesh MI, Wu XC, Dong YL, Wang JH, Gao M, Liu JF, Sun XM (2017) A promising energy storage system: rechargeable Ni–Zn battery. Rare Met 36:381–396. https://doi.org/10.1007/s12598-017-0905-x

Li HB, Gao YQ, Yang GW (2015) Electrochemical route for accessing amorphous mixed-metal hydroxide nanospheres and magnetism. RSC Adv 5:45359–45367. https://doi.org/10.1039/c4ra14370a

Li GC, Liu PF, Liu R, Liu M, Tao K, Zhu SR, Wu MK, Yi FY, Han L (2016) MOF-derived hierarchical double-shelled NiO/ZnO hollow spheres for high-performance supercapacitors. Dalt Trans 45(34):13311–13316. https://doi.org/10.1039/c6dt01791f

Li D, Li Y, Zhao J, Xu Z, Zhang H (2017a) Three-dimensional porous layered double hydroxides growing on carbon cloth as binder-free electrodes for supercapacitors. J Mater Res 32(13):2487–2496. https://doi.org/10.1557/jmr.2017.227

Li J, Wei M, Chu W, Wang N (2017b) High-stable A-phase NiCo double hydroxide microspheres via microwave synthesis for supercapacitor electrode materials. Chem Eng J 316(15):277–287. https://doi.org/10.1016/j.cej.2017.01.057

Liang D, Wu S, Liu J, Tian Z, Liang C (2016) Co-doped Ni hydroxide and oxide nanosheet networks: laser-assisted synthesis, effective doping, and ultrahigh pseudocapacitor performance. J Mater Chem A 4:10609–10617. https://doi.org/10.1039/C6TA03408J

Liu J, Wang J, Zhang X, Fang B, Hu P, Zhao X (2015) Preparation and structural characterization of switterionic surfactant intercalated into NiZn-layerd hydroxide salts. J Phys Chem Solids 85:180–187. https://doi.org/10.1016/j.jpcs.2015.05.017

Lontio Fomekong R, Kenfack Tsobnang P, Magnin D, Hermans S, Delcorte A, Lambi Ngolui J (2015) Coprecipitation of nickel zinc malonata : a facile and reproducible synthesis route for $Ni_{1-x}Zn_xO$ particles and $Ni_{1-x}Zn_xO$/ZnO nanocomposites via pyrolysis. J Solid State Chem 230:381–389. https://doi.org/10.1016/j.jssc.2015.07.040

Mereu RA, Mesaros A, Petrisor T, Gabor M, Popa M, Ciontea L, Petrisor T (2013) Synthesis, characterization and thermal decomposition study of zinc propionate as a precursor for ZnO nanopowders and thin films. J Anal Appl Pyrolys 104:653–659. https://doi.org/10.1016/j.jaap.2013.05.001

Mohamed SG, Attia SY, Allam NK (2017) One-step, calcination-free synthesis of zinc cobaltite nanospheres for high-performance

supercapacitors. Mater Today Energy 4:97–104. https://doi.org/10.1016/j.mtener.2017.04.003

Mohapatra D, Parida S, Badrayyana S, Singh BK (2017) High performance flexible asymmetric CNO-ZnO//ZnO supercapacitor with an operating voltage of 1.8 V in aqueous medium. Appl Mater Today 7:212–221. https://doi.org/10.1016/j.apmt.2017.03.006

Oyedotun KO, Madito MJ, Momodu DY, Mirghni AA, Masikhwa TM, Manyala N (2018) Synthesis of ternary NiCo-MnO_2 nanocomposite and its application as a novel high energy supercapattery device. Chem Eng J 335(1):416–433. https://doi.org/10.1016/j.cej.2017.10.169

Ramadoss A, Kang KN, Ahn HJ, Kim SI, Ryu ST, Jang JH (2016) Realization of high performance flexible wire supercapacitors based on 3-dimensional $NiCo_2O_4$/Ni fibers. J Mater Chem A 4:4718–4727. https://doi.org/10.1039/C5TA10781D

Rojas R, Barriga C, Ulibarri MÁ, Rives V (2004) Intercalation of vanadate in Ni, Zn layered hydroxyacetates. J Solid State Chem 177:3392–3401. https://doi.org/10.1016/j.jssc.2004.05.055

Rojas R, Ángeles Ulibarri M, Barriga C, Rives V (2008) Intercalation of metal-edta complexes in Ni–Zn layered hydroxysalts and study of their thermal stability. Microporous Mesoporous Mater 112:262–272. https://doi.org/10.1016/j.micromeso.2007.09.042

Wang X, Hu J, Liu W, Wang G, An J, Lian J (2015) Ni–Zn binary system hydroxide, oxide and sulfide materials: synthesis and high supercapacitor performance. J Mater Chem A 3:23333–23344. https://doi.org/10.1039/C5TA07169K

Wang S, Wang X, Bao Z, Yang X, Ye L, Zhao L (2017) An evenly distributed sulfur-doped nickel zinc hydroxyl carbonate dispersed structure for all- solid-state asymmetric supercapacitors with enhanced performance. J Mater Chem A 5:10227–10235. https://doi.org/10.1039/C7TA02558K

Xie Q, Ma Y, Zeng D, Wang L, Yue G, Peng DL (2015) Facile fabrication of various zinc-nickel citrate microspheres and their transformation to ZnO–NiO hybrid microspheres with excellent lithium storage properties. Sci Rep 5:8351–8359. https://doi.org/10.1038/srep08351

Zheng S, Xue H, Pang H (2017) Supercapacitors based on metal coordination materials. Coord Chem Rev. https://doi.org/10.1016/j.ccr.2017.07.002

Zhong Z, Li Q, Zhang Y, Zhong H, Cheng M, Zhang Y (2005) Synthesis of nanocrystalline Ni–Zn ferrite powders by refluxing method. Powder Technol 155:193–195. https://doi.org/10.1016/j.powtec.2005.05.060